SPECIAL TOPIC — Smart design of materials and design of smart materials

Thermal transport properties of two-dimensional boron dichalcogenides from a first-principles and machine learning approach

Zhanjun Qiu(邱占均)[1], Yanxiao Hu(胡晏箫)[1], Ding Li(李顶)[1], Tao Hu(胡涛)[1], Hong Xiao(肖红)[1], Chunbao Feng(冯春宝)[1,2,†], and Dengfeng Li(李登峰)[1,2,‡]

[1] *School of Science, Chongqing University of Posts and Telecommunications, Chongqing* 400065, *China*
[2] *Institute for Advanced Sciences, Chongqing University of Posts and Telecommunications, Chongqing* 400065, *China*

(Received 7 December 2022; revised manuscript received 2 February 2023; accepted manuscript online 8 February 2023)

The investigation of thermal transport is crucial to the thermal management of modern electronic devices. To obtain the thermal conductivity through solution of the Boltzmann transport equation, calculation of the anharmonic interatomic force constants has a high computational cost based on the current method of single-point density functional theory force calculation. The recent suggested machine learning interatomic potentials (MLIPs) method can avoid these huge computational demands. In this work, we study the thermal conductivity of two-dimensional MoS_2-like hexagonal boron dichalcogenides (H-B_2VI_2; VI = S, Se, Te) with a combination of MLIPs and the phonon Boltzmann transport equation. The room-temperature thermal conductivity of H-B_2S_2 can reach up to 336 W·m^{-1}·K^{-1}, obviously larger than that of H-B_2Se_2 and H-B_2Te_2. This is mainly due to the difference in phonon group velocity. By substituting the different chalcogen elements in the second sublayer, H-B_2VIVI' have lower thermal conductivity than H-B_2VI_2. The room-temperature thermal conductivity of B_2STe is only 11% of that of H-B_2S_2. This can be explained by comparing phonon group velocity and phonon relaxation time. The MLIP method is proved to be an efficient method for studying the thermal conductivity of materials, and H-B_2S_2-based nanodevices have excellent thermal conduction.

Keywords: boron dichalcogenides, thermal conductivity, machine learning interatomic potentials, first-principles calculation

PACS: 44.10.+i, 63.20.kg, 05.60.Gg, 65.90.+i **DOI:** 10.1088/1674-1056/acb9e6

1. Introduction

Since the discovery of the good thermal transport properties of graphene, the prediction of new two-dimensional (2D) materials with excellent thermal conductivity has attracted much attention.[1–3] With the development of high-frequency, high-integration miniaturized devices, effective heat dissipation is very important for the reliability and performance of systems and we need to find some outstanding thermally conductive materials with different potential applications.

Boron based 2D materials such as boron nitride (BN) and borophene exhibit excellent thermal transport properties.[4–7] From the band structure, we know that BN shows insulating properties and borophene often has metallic properties. Recently, boron dichalcogenides (B_2VI_2, VI = S, Se, Te), a class of 2D MoS_2-like materials, have been reported for potential application in flexible field-effect transistors and excitonic light emitters.[8] Hexagonal (H-) B_2Se_2 exhibits high electron mobility, comparable with that of graphene. H-B_2S_2 is an excellent material for optical nanodevices with a superior refractive index[9] and has excellent hydrogen storage capacity.[10] Its thermal conductance in ballistic thermal transport is calculated to be 2.02 nW·K^{-1}·nm^{-1},[11] which is comparable to that of borophene and larger than that of graphene.[12,13] The thermal conductivity of the diffusion transport of H-B_2VI_2 is not yet known and is important for the application of H-B_2VI_2-based devices.

As a general method for calculating thermal conductivity, solution of the phonon Boltzmann transport equation (PBTE) requires the harmonic and anharmonic interatomic force constants (IFCs), which are commonly acquired by density functional theory (DFT) calculations over supercell lattices with finite atomic displacements.[14,15] In most cases, we require hundreds or thousands of single-point DFT force calculations to obtain the anharmonic IFCs. Additionally, this large number of calculations have to be repeated for different cutoff distances. Therefore, the computational cost for calculating the anharmonic IFCs is very high. Machine learning is a new method that has recently been applied to multiple areas, including the calculation of the interatomic potential of materials.[16–18] The moment tensor potential (MTP),[19,20] one type of machine learning potential, is used to obtain the interatomic potential during supervised learning. The anharmonic IFCs can be obtained without single-point DFT force

†Corresponding author. E-mail: lidf@cqupt.edu.cn
‡Corresponding author. E-mail: fengcb@cqupt.edu.cn

© 2023 Chinese Physical Society and IOP Publishing Ltd

calculations. Compared with the DFT-based solution, this method does not need repeated calculation due to the variation of cutoff distance. Its high accuracy and effectiveness have already been demonstrated in thermal conductivity calculations for several materials.[21,22]

In this work we investigate the phonon transport properties of H-B_2VI_2 with a combination of the machine learning interatomic potential (MLIP) and PBTE. B_2S_2 is found to have a high lattice thermal conductivity, and its harmonic nature results in the difference in thermal conductivity for H-B_2VI_2. Substituting the VI atoms in the second sublayer with different chalcogen elements in H-B_2VI_2 we propose another three types of unsymmetrical boron dichalcogenide. We find that the thermal conductivity is obviously reduced.

2. Computational method

All the first-principles calculations based on DFT in our work are performed using the Vienna *ab initio* simulation package (VASP).[23,24] The generalized gradient approximation (GGA) of the Perdew–Burke–Ernzerhof (PBE)[25] exchange–correlation function is used. The kinetic cutoff energy is set to 550 eV. For the relaxation of all structures, a $17\times17\times1$ k-point gamma-centered method is used to sample the Brillouin zone. The convergence criteria for energies and atomic force are 10^{-7} eV and 0.00001 eV·Å^{-1}, respectively. A vacuum space of 20 Å is chosen to avoid interaction between adjacent layers.

In the *ab initio* molecular dynamics (AIMD) calculation, the canonical ensemble (NVT) was performed for an $8\times8\times1$ conventional supercell at 100 K, 300 K, 500 K, and 700 K with a time step of 1 fs and a total step of 300; thus 2100 structures were obtained. A gamma-centered grid of $3\times3\times1$ was used in the AIMD calculation. The second- and third-order interatomic force constants were obtained by using MLIPs[26] with the well-trained MTP, with PHONOPY software[27] and thirdorder.py script.[28] The same supercell ($8\times8\times1$) is used for the calculation of harmonic and anharmonic force constants on account of the negligible cost.

MTP[19,20] is a local potential with an energy which is the summation of contributions of local neighborhoods m_i of each atom, expressed as

$$E^{\mathrm{mtp}}(\mathrm{cfg})=\sum_i V(m_i). \tag{1}$$

Here, i ranges from 1 to the number of atoms in the local environment and m_i is a collection including the interatomic vector between the central atom and neighboring atoms within a cutoff radius and their atomic types. Furthermore, the function V can be expressed as a linear combination of a set of basis functions B_α:

$$V(m_i)=\sum_\alpha^n \eta_\alpha B_\alpha(m_i), \tag{2}$$

where $\eta=\{\eta_\alpha\}$ are the parameters of the MLIP.

The functional form of B_α is described by moment tensor descriptors $M_{\mu,\nu}(m_i)$, given as

$$M_{\mu,\nu}(m_i)=\sum_j f_\mu(|r_{ij}|,z_i,z_j)r_{ij}^{\otimes\nu}. \tag{3}$$

The angular part $r_{ij}^{\otimes\nu}$ contains angular information about the neighborhood n_i, and $\otimes\nu$ is the νth power outer product of r_{ij}. For the radial part $f_\mu(|r_{ij}|z_i,z_j)$ of the MTP, $|r_{ij}|$, z_i and z_j are the distance between atoms i and j and their atomic types, respectively. It can be expanded by a set of radial basis functions Q_λ:

$$f_\mu(|r_{ij}|,z_i,z_j)=\sum_{\lambda=1}^{N_Q} c_\mu(S_i,S_j,\lambda)Q_\lambda(|r_{ij}|), \tag{4}$$

where $c_\mu(S_i,S_j,\lambda)$ are the radial coefficients (parameters) and

$$Q_\lambda(|r_{ij}|)=\begin{cases}\varphi_\lambda(|r_{ij}|)(R_{\mathrm{cut}}-r_{ij})^2, & |r_{ij}|<R_{\mathrm{cut}},\\ 0, & |r_{ij}|\geq R_{\mathrm{cut}},\end{cases} \tag{5}$$

the radial basis functions are available in the form of $\varphi_\lambda(|r_{ij}|)(R_{\mathrm{cut}}-r_{ij})^2$ only when $|r_{ij}|$ stays below the cutoff radius. φ_λ is the polynomial function on the interval from the minimum atomic distance (R_{min}) to the cutoff radius (R_{cut}) in the investigated system.

The size of the radial basis N_Q which is defined as the radial part of moment tensor descriptors, and the level of the MTP, $\mathrm{lev}_{\mathrm{max}}$, determine the basis function B_α.[26] With regard to the accuracy and training efficiency we must select a suitable size of N_Q. Therefore, 18 was set as the maximum level of moments; then the value of B_α and the size of the radial basis are 163 and 8, respectively. To ensure the accuracy of the MTP, the cutoff radius was set to 7 Å.

The thermal transport of semiconductors and insulators is dominated by phonons, and can be expressed as

$$\kappa_{\alpha\beta}=\frac{1}{k_{\mathrm{B}}T^2NV}\sum_\lambda\left(1+f_\lambda^0\right)f_\lambda^0(\hbar\omega_\lambda)^2v_\lambda^\alpha v_\lambda^\beta\tau_\lambda, \tag{6}$$

where k_{B}, T, N, V, f_λ^0, $\hbar$, ω, v, and τ are the Boltzmann constant, absolute temperature, the number of wave vector q points in the Brillouin zone, the equilibrium Boltzmann distribution, the reduced Planck constant, the angular frequency, phonon group velocity and phonon relaxation time, respectively. The indices α, β, and λ denote vector direction and mode index of the phonon. The phonon relaxation time, the inverse of which equals the sum of anharmonic scattering and isotope scattering, is obtained from the Fermi golden rule. The phonon thermal conductivity is calculated by ShengBTE code[28] by solving the PBTE with a $101\times101\times1$ q-mesh via an iterative method. In order to obtain the convergence of thermal conductivity, we considered the cutoff of interactions up to 0.7 nm in the calculation of third-order force constants.

3. Result and discussion

3.1. Thermal conductivity of H-B_2VI_2

Figures 1(a) and 1(b) show the top and side views of H-B_2VI_2 monolayer structures. They have the *P6m*2 space group. The optimized lattice constants, effective thicknesses and bond lengths of these structures are presented in Table 1. We find that the lattice constant and B–*VI* bond length become larger with increasing atomic mass. The lattice constant of H-B_2S_2 is calculated to be 3.044 Å, and the lengths of the B–B and B–S bonds are 1.728 Å and 1.952 Å, respectively. These results are in good agreement with previous calculations.[8] For H-B_2Te_2, the lattice constant and B–Te bond length are 3.565 Å and 2.314 Å, respectively. Figures 1(d)–1(f) show the electron localization function (ELF) of H-B_2VI_2. The value of the ELF ranges from 0 to 1, which means electrons become more localized in that region. We can see that the B–B bond exhibits a stronger covalent property than B–*VI* bonds. Additionally, we calculate the mechanical properties of H-B_2VI_2. The elastic constants (C_{ij}) are obtained based on the energy–strain method,[29] and the Poisson's ratio and in-plane Young's modulus (Y_{2D}) are calculated via elastic constants, as seen in Table 2. H-B_2S_2 has the largest Young's modulus and H-B_2Te_2 has the largest Poisson's ratio. From the results for elastic constants, we can see that they satisfy the elastic stability conditions of 2D hexagonal crystals,[30] namely, $C_{11} > 0$ and $C_{11} > |C_{12}|$. The mechanical stability of H-B_2VI_2 is confirmed.

To study the dynamic stability, we present the phonon dispersion spectrum of H-B_2VI_2, as shown in Figs. 2(a)–2(c). There is no imaginary frequency mode, indicating that these structures are dynamically stable. The phonon dispersion spectrum is similar due to the similar structures. There are four atoms in each unit cell and three acoustic and nine optical phonon branches. Due to the large atomic mass ratio, the whole phonon dispersion is divided into three parts by two band gaps. The low-frequency bunched region of acoustic and optical branches, which is dominated by heavy atoms, becomes narrowed with increasing of the mass of the chalcogen atom. This implies that H-B_2S_2 has a larger phonon group velocity. From the phonon density of states (PDOS) of the three structures, we can see that the high- and low-frequency phonon modes are mainly contributed by boron atoms and *VI* atoms, respectively. In the middle-frequency range, the phonon modes of H-B_2Se_2 and H-B_2Te_2 come from Se and Te atoms while those for H-B_2S_2 are derived from B and S atoms, originating from the difference in atomic mass. Moreover, to validate the accuracy of MTPs in describing the interatomic interactions, the phonon dispersions of our studied structures calculated by DFT are compared with MTP-based results in Figs. 2(a)–2(f) (red dotted lines). This indicates that the results are in excellent agreement, which confirms the reliability of our MTP-based calculations.

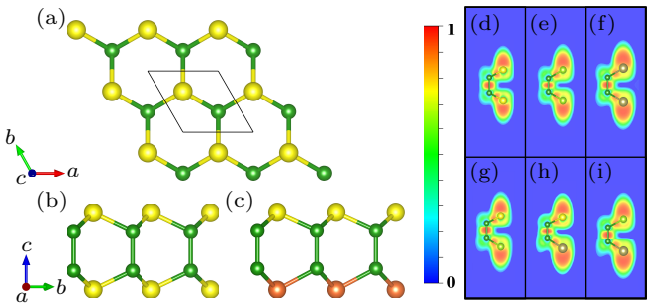


Fig. 1. Optimized (a) top and (b) side views of H-B_2VI_2 (VI = S, Se, Te) monolayers. (c) Side views of H-B_2VIVI' (VI' = S, Se, Te) monolayers. The electron localization function maps of H-B_2VI_2 and H-B_2VIVI': (d) B_2S_2, (e) B_2Se_2, (f) B_2Te_2, (g) B_2SSe, (h) B_2STe, (i) B_2SeTe. The green and yellow balls represent boron and *VI*-group atoms, respectively, and the black frames are the primitive cells.

Table 1. The lattice constants, effective thickness, bond length of hexagonal boron dichalcogenide monolayers.

Structure	Lattice constant (Å)	Effective thickness (Å)	Bond length (Å)		
			B–B	B–VI_1	B–VI_2
H-B_2S_2	3.044	7.070	1.728	1.952	–
H-B_2Se_2	3.256	7.466	1.713	2.105	–
H-B_2Te_2	3.565	8.290	1.713	2.314	–
H-B_2SSe	3.153	7.268	1.719	2.002	2.061
H-B_2SeTe	3.420	7.880	1.708	2.181	2.254
H-B_2STe	3.328	7.686	1.707	2.088	2.219

Table 2. The band gap (eV), elastic constants (C_{ij}), in-plane Young's modulus (Y_{2D}) and Poisson's ration of hexagonal boron dichalcogenide monolayers.

Structure	Band gap (eV)	$C_{11} = C_{22}$ (N·m^{-1})	C_{12} (N·m^{-1})	C_{66} (N·m^{-1})	Y_{2D} (N·m^{-1})	Poisson's ratio
H-B_2S_2	3.910	218.430	26.868	95.781	215.125	0.123
H-B_2Se_2	3.466	178.300	26.357	75.972	174.404	0.148
H-B_2Te_2	2.137	142.632	22.125	60.254	139.200	0.155
H-B_2SSe	3.493	194.929	28.013	83.458	190.904	0.144
H-B_2SeTe	2.405	153.660	25.438	64.111	149.449	0.166
H-B_2STe	2.116	158.413	31.156	63.628	152.285	0.197

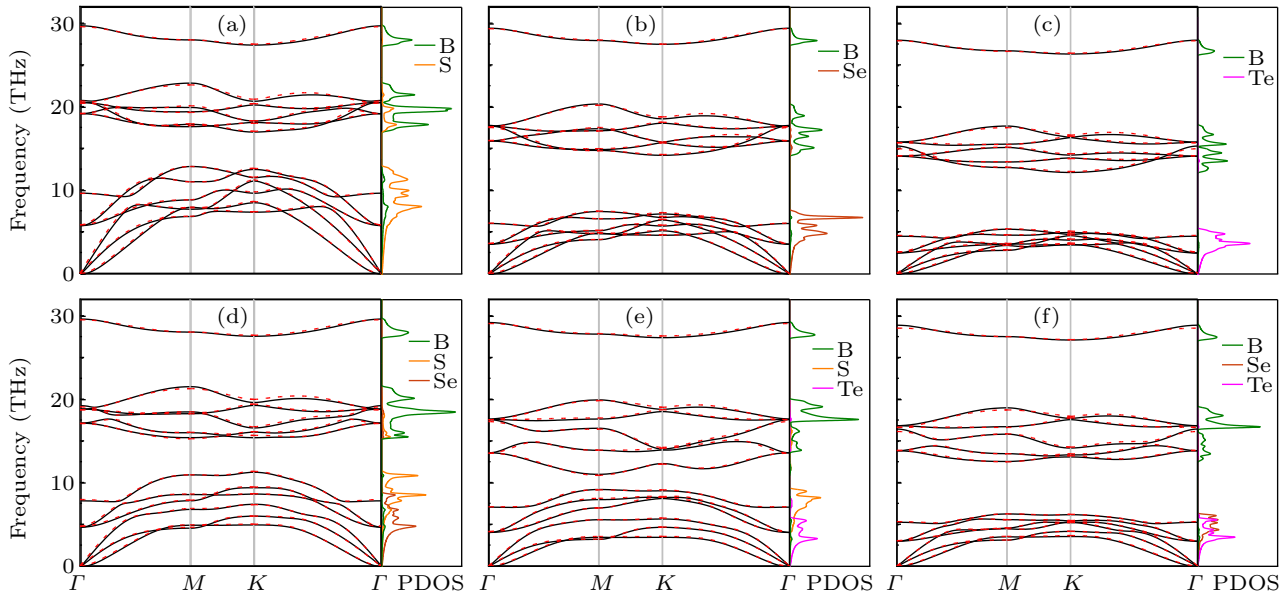


Fig. 2. Phonon dispersion relations and phonon density of states (PDOS) of (a) H-B_2S_2, (b) H-B_2Se_2, (c) H-B_2Te_2, (d) H-B_2SSe, (e) H-B_2STe and (f) H-B_2SeTe are calculated by the density functional theory (black continuous lines) and moment tensor potential (red dotted lines) methods.

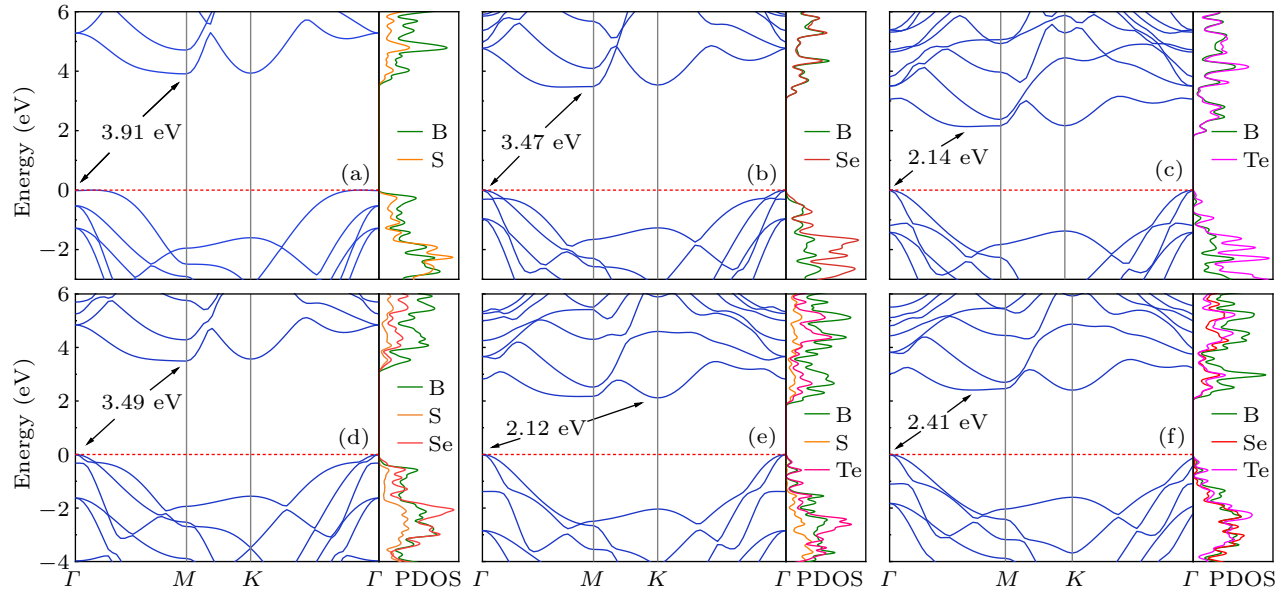


Fig. 3. Band structures and density of states of (a) H-B_2S_2, (b) H-B_2Se_2, (c) H-B_2Te_2, (d) H-B_2SSe, (e) H-B_2STe and (f) H-B_2SeTe from hybrid functional of Heyd, Scuseria and Ernzerhof calculations. The Fermi energy is set to zero. PDOS, phonon density of states.

From the calculation results for the hybrid functional of Heyd, Scuseria and Ernzerhof in Fig. 3 we find that the band gap of H-B_2VI_2 is larger than 2 eV. The contribution to the thermal transport mainly comes from lattice vibrations and that from electrons can be neglected. Based on the PBTE method, the calculated lattice thermal conductivities (κ) of H-B_2VI_2 are plotted in Fig. 4. This shows that the thermal conductivities of the three structures are isotropic and decrease with increasing temperature due to stronger phonon scattering. The lattice thermal conductivity of B_2S_2 is larger than that of B_2Se_2 and B_2Te_2, as expected from the phonon dispersion analysis above. At room temperature, the lattice thermal conductivity of B_2S_2 can reach up to 336 $W{\cdot}m^{-1}{\cdot}K^{-1}$, which is about twice that of B_2Se_2 (189 $W{\cdot}m^{-1}{\cdot}K^{-1}$) and nearly four times that of B_2Te_2 (89 $W{\cdot}m^{-1}{\cdot}K^{-1}$). This value also exceeds that for most 2D semiconducting materials such as Mg_2C (5 $W{\cdot}m^{-1}{\cdot}K^{-1}$–20 $W{\cdot}m^{-1}{\cdot}K^{-1}$),[31] silicene (9 $W{\cdot}m^{-1}{\cdot}K^{-1}$–26 $W{\cdot}m^{-1}{\cdot}K^{-1}$),[32,33] honeycomb boron arsenide ($\sim$ 181 $W{\cdot}m^{-1}{\cdot}K^{-1}$)[34] and $MoSe_2$ (59 ± 18 $W{\cdot}m^{-1}{\cdot}K^{-1}$).[3] Moreover, the room-temperature thermal conductivity of B_2S_2 from the MTP method is comparable with that from the DFT-based method (373 $W{\cdot}m^{-1}{\cdot}K^{-1}$), confirming the reliability of our MTP method. To explore the thermal transport properties of H-B_2VI_2, we extract the contribution of acoustic branches and optical branches, as shown in Fig. 8. We find that the main contribution to the thermal conductivity of these structures at room temperature is from the acoustic branches. In addition, the out-of-plane flexural acous-

tic (ZA) branch plays a dominant role in thermal transport due to the horizontal reflection symmetry based three-phonon selection rule.[35]

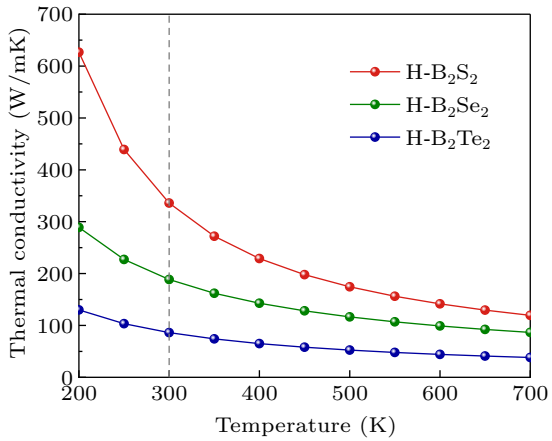


Fig. 4. Temperature-dependent lattice thermal conductivity of hexagonal boron dichalcogenide monolayers.

The lattice thermal conductivity depends on the phonon group velocity and phonon scattering rates based on the phonon gas model and kinetic theory. As shown in Fig. 5, the phonon group velocity of B_2S_2 is obviously larger than that of B_2Se_2 and B_2Te_2, with that of B_2Te_2 being the lowest. At the same time, the phonon relaxation time of the three structures is comparable. Therefore, the major factor behind the difference in thermal conductivity of the three compounds is their harmonic nature.

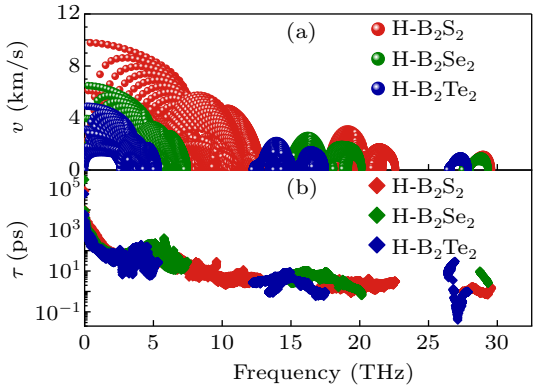


Fig. 5. Frequency-dependent (a) phonon group velocity (v) and (b) phonon relaxation time (τ) of hexagonal boron dichalcogenide monolayers.

3.2. Effect of substitutions on the lattice thermal conductivity of H-B_2VI_2

When all the VI atoms in the second sublayer are substituted by different chalcogen elements in H-B_2VI_2, H-B_2VIVI' is formed; the structure is as shown in Fig. 1(c). The substitution spoils the mirror symmetry in H-B_2VI_2. The electron localization function of H-B_2VIVI' is plotted in Figs. 1(g)–1(i), confirming the significant covalent bonding character. The structural parameters and mechanical properties of H-B_2VIVI' are presented in Tables 1 and 2, respectively. We can see that the calculated lattice constant and Young's modulus of ternary boron chalcogenides compare with their binary boron dichalcogenide structure, which consist of partial ternary component elements. However, the Poisson's ratio of these ternary compound is larger than that of the binary ones, especially for B_2STe, for which the value of Poisson's ratio is about 60% larger than that of B_2S_2. From the calculated elastic constants and the phonon dispersion spectrum of H-B_2VIVI', we find that these structures satisfy the criteria for mechanical and thermodynamic stability.

The phonon dispersion spectrum and PDOS of H-B_2VIVI' are presented in Figs. 2(d)–2(f), showing that the acoustic phonon modes tend to lower frequency with substitution by the heavier atoms; this can suppress the thermal conductivity. Comparing the phonon dispersion of B_2S_2 and B_2STe, the maximum acoustic branches frequency of B_2STe is 5.68 THz, which is smaller that of B_2S_2 (11.16 THz). The overlap of acoustic phonon branches and optical phonon branches in B_2S_2 vanishes in B_2STe. The acoustic phonon modes of B_2S_2 mainly stem from the S atoms, while those for B_2STe are from the Te atoms. In addition, in the middle-frequency range, S atoms contribute to the phonon modes in H-B_2S_2 while the phonon modes for B_2STe mainly stem from the B atoms with hardly any contribution from S atoms.

Figure 6 compares the room-temperature thermal conductivity of H-B_2VIVI' and H-B_2VI_2. It can be seen that the thermal conductivity of H-B_2VIVI' is obviously smaller than that for H-B_2VI_2, with the lowest value being only 37 $W{\cdot}m^{-1}{\cdot}K^{-1}$ for B_2STe. With the partial substitution of S by Te in H-B_2S_2, the room-temperature thermal conductivity deceases to only 11% of that of H-B_2S_2. The κ value for H-B_2VIVI' is smaller than that of H-B_2VI_2 and H-B_2VI_2' but the average atomic mass of H-B_2VIVI' is not the heaviest. Similarly, the κ value for B_2STe is about half of that of B_2SeTe although its average atomic mass is smaller. Based on the Slack criteria, the material with the lighter average atomic mass has a larger thermal conductivity. To understand the mechanics of the change in thermal conductivity with the substitution, we compare the phonon group velocity and scattering rates in

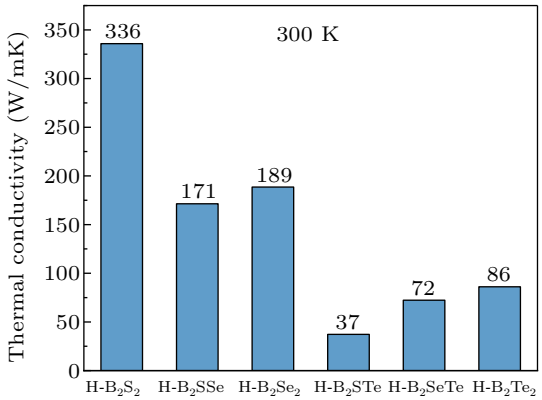


Fig. 6. Lattice thermal conductivity of hexagonal boron dichalcogenide monolayers at room temperature.

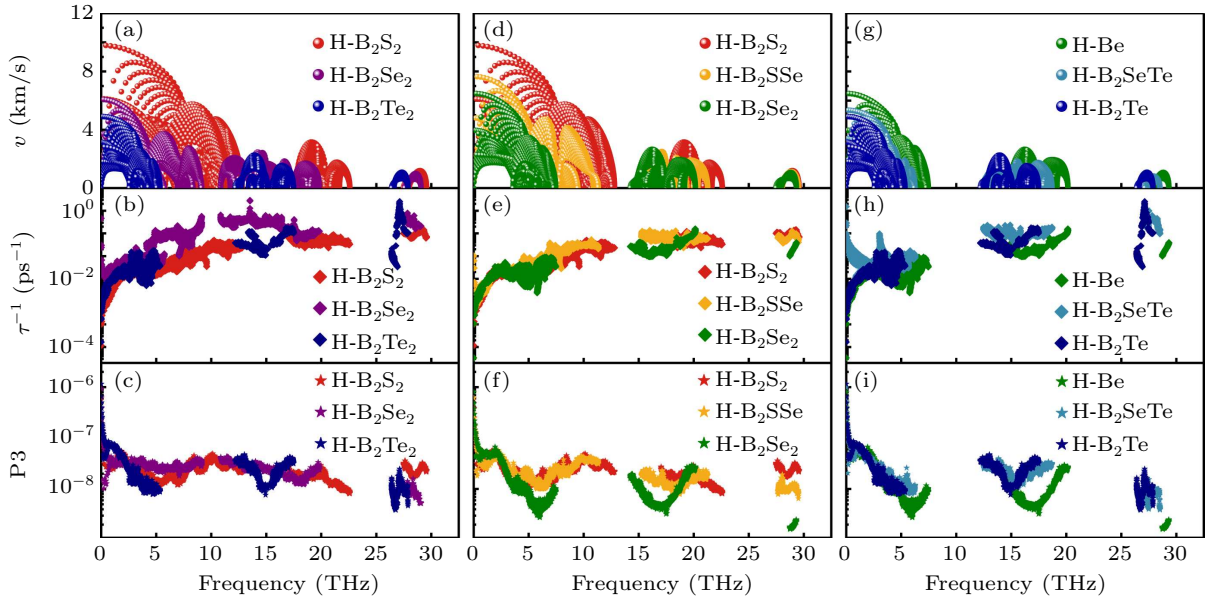


Fig. 7. Frequency-dependent (a) phonon group velocity, (b) scattering rate and (c) phase space of H-B_2S_2, H-B_2Te_2 and H-B_2STe monolayers. Frequency-dependent (d) phonon group velocity, (e) scattering rate and (f) phase space of H-B_2S_2, H-B_2Se_2 and H-B_2SSe monolayers. Frequency-dependent (g) phonon group velocity, (h) scattering rate and (i) phase space of H-B_2Se_2, H-B_2Te_2 and H-B_2SeTe monolayers.

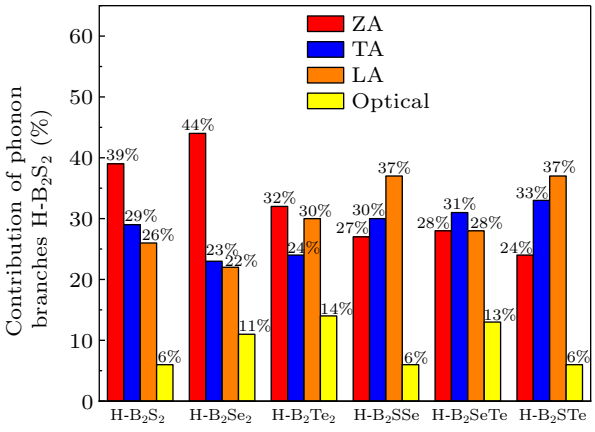


Fig. 8. Percentage contribution to thermal conductivity from out-of-plane flexural acoustic (ZA), transverse acoustic (TA), longitudinal acoustic (LA) and optical phonon modes of hexagonal boron dichalcogenide monolayers.

Fig. 7. For B_2SSe and B_2STe, with substitution of S by Se and Te in B_2S_2 the phonon group velocities are obviously smaller than that of B_2S_2 and they have higher phonon scattering rates than B_2S_2. This results in a significant reduction in the thermal conductivity of B_2S_2. In Figs. 7(a) and 7(b), B_2STe, which has the lowest κ value, possesses a larger phonon group velocity than B_2Te_2. The change of thermal conductivity cannot be understood from the phonon group velocity. Fortunately, the phonon scattering rate of B_2Te_2 is much lower than that of B_2STe, especially in the region of 4 THz–17 THz, indicating that the lower κ in B_2STe is mainly due to the stronger anharmonicity attributable to their different phonon dispersion spectra. On the one hand, in B_2Te_2, acoustic branches are narrowed by the heavy atomic mass of Te and entangled in low-frequency regions (about 0 THz–4 THz). The phase space of the aaa phonon scattering process is decreased by bunching of the acoustic branches (as shown in Fig. 7(c)), which is governed by the energy conservation condition. On the other hand, the huge energy gap in the low-frequency region shown in B_2Te_2 is sharply contracted in B_2STe, resulting in an expanding region for phonon branches. This behavior enhances the aao phonon scattering process and eventually reduces the phonon relaxation time of B_2STe. Likewise, in the other two H-B_2VIVI' we also find a similar phenomenon [plotted in Figs. 7(d)–7(f) and 7(g)–7(i)]. Moreover, the contribution of different acoustic branches and optical branches to the thermal conductivity of H-B_2VIVI' is presented in Fig. 8. Unlike H-B_2VI_2, ZA branches do not play a dominant role in thermal transport due to the destruction of mirror symmetry. For B_2STe and B_2SSe, longitudinal acoustic modes appear to make the main contribution to thermal transport. The three acoustic modes have a comparable role in the thermal transport of B_2SeTe.

4. Conclusion

In this paper we have performed an investigation into the lattice thermal conductivity of six kinds of hexagonal boron dichalcogenide by solving the PBTE based on the MLIPs method. This approach can give the anharmonic interatomic force constants without a large computational cost and avoids the repeated calculations for setting different cutoff distances. We predict that H-B_2S_2 has a high thermal conductivity with a value of 337 $W{\cdot}m^{-1}{\cdot}K^{-1}$ at 300 K. It was found that the substitution of different chalcogen elements (H-B_2VIVI') can substantially decrease the thermal conductivity of H-B_2VI_2. The room-temperature thermal conductivity of B_2STe is only 11% of that of H-B_2S_2. These results were explained in de-

tail by comparing phonon group velocity and phonon relaxation time. This work provides information for future studies of thermal conductivity of materials with an efficient method and for the design H-B_2S_2-based nanodevices with high thermal conduction.

Acknowledgments

Project supported by Scientific and Technological Research of Chongqing Municipal Education Commission (Grant No. KJZD-K202100602) and the funding of Institute for Advanced Sciences of Chongqing University of Posts and Telecommunications (Grant No. E011A2022326).

References

[1] Balandin A A 2011 *Nat. Mater.* **10** 569
[2] Cai W, Moore A L, Zhu Y, Li X, Chen S, Shi L and Ruoff R S 2010 *Nano Lett.* **10** 1645
[3] Zhang X, Sun D, Li Y, Lee G H, Cui X, Chenet D, You Y, Heinz T F and Hone J C 2015 *ACS Appl. Mater. Interfaces* **7** 25923
[4] Fan H, Wu H, Lindsay L and Hu Y 2019 *Phys. Rev. B* **100** 085420
[5] Li D, Gao J, Cheng P, He J, Yin Y, Hu Y, Chen L, Cheng Y and Zhao J 2020 *Adv. Funct. Mater.* **30** 1904349
[6] Hu Y, Yin Y, Li S, Zhou H, Li D and Zhang G 2020 *Nano Lett.* **20** 7619
[7] Li D, Chen Y, He J, Tang Q, Zhong C and Ding G 2018 *Chin. Phys. B* **27** 036303
[8] Tang C, Ma F, Zhang C, Jiao Y, Matta S K, Ostrikov K and Du A 2019 *J. Mater. Chem. C* **7** 1651
[9] Mishra P, Singh D, Sonvane Y and Ahuja R 2020 *AIP Conf. Proc.* **2220** 130039
[10] Mishra P, Singh D, Sonvane Y and Ahuja R 2020 *J. Appl. Phys.* **127** 184305
[11] Çınar M N, Sargın G Ö, Sevim K, Özdamar B, Kurt G and Sevinçli H 2021 *Phys. Rev. B* **103** 165422
[12] Li D, He J, Ding G, Tang Q, Ying Y, He J, Zhong C, Liu Y, Feng C and Sun Q 2018 *Adv. Funct. Mater.* **28** 1801685
[13] He J, Li D, Ying Y, Feng C, He J, Zhong C, Zhou H, Zhou P and Zhang G 2019 *NPJ Comput. Mater.* **5** 1
[14] Parlinski K, Li Z and Kawazoe Y 1997 *Phys. Rev. Lett.* **78** 4063
[15] Li W, Lindsay L, Broido D A, Stewart D A and Mingo N 2012 *Phys. Rev. B* **86** 174307
[16] Behler J and Parrinello M 2007 *Phys. Rev. Lett.* **98** 146401
[17] Bartók A P, Payne M C, Kondor R and Csányi G 2010 *Phys. Rev. Lett.* **104** 136403
[18] Korotaev P, Novoselov I, Yanilkin A and Shapeev A 2019 *Phys. Rev. B* **100** 144308
[19] Shapeev A V 2016 *Multiscale Model. Simul.* **14** 1153
[20] Gubaev K, Podryabinkin E V and Shapeev A V 2018 *J. Chem. Phys.* **148** 241727
[21] Mortazavi B, Podryabinkin E V, Novikov I S, Rabczuk T, Zhuang X and Shapeev A V 2021 *Comput. Phys. Commun.* **258** 107583
[22] Liu Z, Yang X, Zhang B and Li W 2021 *ACS Appl. Mater. Interfaces* **13** 53409
[23] Kresse G and Furthmüller J 1996 *Phys. Rev. B* **54** 11169
[24] Kresse G and Hafner J 1994 *Phys. Rev. B* **49** 14251
[25] Perdew J P, Burke K and Ernzerhof M 1996 *Phys. Rev. Lett.* **77** 3865
[26] Novikov I S, Gubaev K, Podryabinkin E V and Shapeev A V 2020 *Mach. Learn.: Sci. Technol.* **2** 025002
[27] Togo A and Tanaka I 2015 *Scripta Mater.* **108** 1
[28] Li W, Carrete J, Katcho N A and Mingo N 2014 *Comput. Phys. Commun.* **185** 1747
[29] Le Page Y and Saxe P 2001 *Phys. Rev. B* **63** 174103
[30] Born M and Huang K 1954 *Dynamical Theory of Crystal Lattices* (1nd edn.) (New York: Oxford University Press) pp. 129–165
[31] Wang H, Zhou E, Duan F, Wei D, Zheng X, Tang C, Ouyang T, Yao Y, Qin G and Zhong J 2021 *J. Phys. Chem. Lett.* **12** 10353
[32] Xie H, Hu M and Bao H 2014 *Appl. Phys. Lett.* **104** 131906
[33] Gu X and Yang R 2015 *J. Appl. Phys.* **117** 025102
[34] Hu Y, Yin Y, Ding G, Liu J, Zhou H, Feng W, Zhang G and Li D 2021 *Mater. Today Phys.* **17** 100346
[35] Lindsay L, Broido D and Mingo N 2010 *Phys. Rev. B* **82** 115427